Article

Scalable spin squeezing in a dipolar Rydberg atom array

https://doi.org/10.1038/s41586-023-06414-9

Received: 14 March 2023

Accepted: 7 July 2023

Published online: 30 August 2023

Check for updates

Guillaume Bornet[1,7], Gabriel Emperauger[1,7], Cheng Chen[1,7]✉, Bingtian Ye[2,7], Maxwell Block[2,7], Marcus Bintz[2], Jamie A. Boyd[1], Daniel Barredo[1,3], Tommaso Comparin[4], Fabio Mezzacapo[4], Tommaso Roscilde[4], Thierry Lahaye[1], Norman Y. Yao[2,5,6] & Antoine Browaeys[1]

The standard quantum limit bounds the precision of measurements that can be achieved by ensembles of uncorrelated particles. Fundamentally, this limit arises from the non-commuting nature of quantum mechanics, leading to the presence of fluctuations often referred to as quantum projection noise. Quantum metrology relies on the use of non-classical states of many-body systems to enhance the precision of measurements beyond the standard quantum limit[1,2]. To do so, one can reshape the quantum projection noise—a strategy known as squeezing[3,4]. In the context of many-body spin systems, one typically uses all-to-all interactions (for example, the one-axis twisting model[4]) between the constituents to generate the structured entanglement characteristic of spin squeezing[5]. Here we explore the prediction, motivated by recent theoretical work[6–10], that short-range interactions—and in particular, the two-dimensional dipolar XY model—can also enable the realization of scalable spin squeezing. Working with a dipolar Rydberg quantum simulator of up to $N = 100$ atoms, we demonstrate that quench dynamics from a polarized initial state lead to spin squeezing that improves with increasing system size up to a maximum of -3.5 ± 0.3 dB (before correcting for detection errors, or roughly -5 ± 0.3 dB after correction). Finally, we present two independent refinements: first, using a multistep spin-squeezing protocol allows us to further enhance the squeezing by roughly 1 dB, and second, leveraging Floquet engineering to realize Heisenberg interactions, we demonstrate the ability to extend the lifetime of the squeezed state by freezing its dynamics.

The past decade has witnessed the use of squeezed states of light and spin ensembles to improve on a multitude of applications, ranging from gravitational wave detectors[11] and atom interferometers[12] to optical atomic clocks[13,14]. The realization of spin squeezing by means of global interactions has been demonstrated using a variety of platforms, including atomic vapours coupled to light, trapped ions, ultracold gases and cavity quantum electrodynamics[2]. Whether short-range interaction (decaying as a power of the distance larger than the dimensionality) can yield scalable spin squeezing has remained an essential open question[6,15,16]. Recent theoretical advances point to an affirmative answer[6–10,17], proposing a deep connection between spin squeezing and continuous symmetry breaking (CSB)[7,9,10,18]. This connection to CSB order broadens the landscape of systems expected to show scalable spin squeezing, and suggests that both power-law interactions and nearest-neighbour couplings can lead to sensitivity beyond the standard quantum limit (SQL)[9,10]. Of particular relevance is the ferromagnetic, dipolar XY model; indeed, this model is naturally realized in several quantum simulation platforms ranging from ultracold molecules[19–22] and solid-state spin defects[23] to Rydberg atom arrays[24,25].

In this work, we demonstrate the generation of spin-squeezed states using a square lattice of up to $N = 100$ Rydberg atoms. Our main results are threefold. First, we explore the quench dynamics of an initially polarized spin state evolving under the dipolar XY model, using a procedure analogous to the one introduced for the case of all-to-all interactions[4]. We show that the resulting state shows spin squeezing and characterize the generation of multipartite entanglement as a function of time. Moreover, the squeezing improves with increasing system size, providing evidence for the existence of scalable spin squeezing. Second, we introduce a multistep approach to squeezing, where the quench dynamics are interspersed with microwave rotations. We demonstrate that this technique leads to an improvement in the amount of spin squeezing and also enables the squeezing to persist to longer time scales. Finally, motivated by metrological applications, we show that it is possible to freeze the squeezing dynamics (for example, when accumulating a signal) by performing Floquet engineering. In particular, we transform the dipolar XY model into a dipolar Heisenberg model[26,27], so that the squeezing remains constant in time.

[1]Charles Fabry Laboratory University of Paris-Saclay, Institute of Optics Graduate School, CNRS, Palaiseau Cedex, France. [2]Department of Physics, Harvard University, Cambridge, MA, USA. [3]Nanomaterials and Nanotechnology Research Center (CINN-CSIC), University of Oviedo (UO), El Entrego, Spain. [4]Laboratory of Physics, University of Lyon, Ens de Lyon, CNRS, Lyon, France. [5]Department of Physics, University of California, Berkeley, CA, USA. [6]Materials Sciences Division, Lawrence Berkeley National Laboratory, Berkeley, CA, USA. [7]These authors contributed equally: Guillaume Bornet, Gabriel Emperauger, Cheng Chen, Bingtian Ye, Maxwell Block. ✉e-mail: cheng.chen@institutoptique.fr

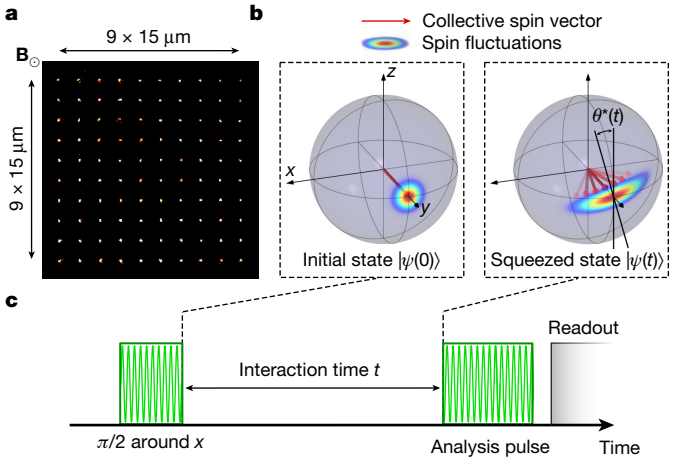

Fig. 1 | Generation of spin-squeezed states in a dipolar Rydberg atom array. a, Fluorescence image of a fully assembled 10×10 ^{87}Rb array. **b**, Spin fluctuations represented through the Husimi Q distributions (coloured area)^2 of the initial coherent-spin state $|\rightarrow\cdots\rightarrow\rangle$ (left panel) and of a squeezed state obtained during the dynamics (right panel), depicted on a generalized Bloch sphere. The angle $\theta^*(t)$ corresponds to the direction of the narrowest noise distribution. The squeezed state is schematically depicted by a superposition of coherent states (red arrows). **c**, The sequence of microwave pulses corresponding to the spin-squeezing protocol. A first $\pi/2$ pulse initializes all the spins along $\hat{y}$. By tuning the duration and phase of a second (analysis) microwave pulse before readout, one can rotate the spin distribution around $\hat{y}$ to measure the variance $\mathrm{Var}(J_\theta)$ along any direction θ, or around $\hat{x}$ to measure the spin length $|\langle J_y\rangle|$.

Our experimental setup[28] consists of a two-dimensional (2D) square array of ^{87}Rb atoms trapped in optical tweezers (Fig. 1a). To implement the dipolar XY model[29], we rely on resonant dipole–dipole interactions between two Rydberg states of opposite parities. In particular, we encode an effective spin-1/2 degree of freedom as $|\uparrow\rangle = |60S_{1/2}, m_j = +1/2\rangle$ and $|\downarrow\rangle = |60P_{3/2}, m_j = -1/2\rangle$, leading to an interaction Hamiltonian:

$$H_{\mathrm{XY}} = -\frac{J}{2}\sum_{i<j}\frac{a^3}{r_{ij}^3}(\sigma_i^x\sigma_j^x + \sigma_i^y\sigma_j^y), \qquad (1)$$

where $\sigma_i^{x,y,z}$ are Pauli matrices, r_{ij} is the distance between spins i and j, $J/h = 0.25$ MHz is the dipolar interaction strength and $a = 15$ μm is the lattice spacing. A magnetic field perpendicular to the lattice plane defines the quantization axis and ensures that the dipolar interactions are isotropic.

We begin by investigating the squeezing dynamics generated by H_{XY}. The atoms are initially excited from the ground state to the Rydberg state $|\uparrow\rangle$, using stimulated Raman adiabatic passage (Methods). Using a microwave $\pi/2$ pulse tuned to the transition between the spin states, we prepare an initial coherent-spin state along the y axis, $|\psi(0)\rangle = |\rightarrow\cdots\rightarrow\rangle$ (Fig. 1b). Next, we allow the system to evolve under H_{XY} and measure the squeezing as a function of time.

As squeezing manifests as a change in the shape of the noise distribution, one must measure the variance of the collective-spin operator in the plane perpendicular to the mean-spin direction; to this end, we define $J_\theta = \cos(\theta)J_z + \sin(\theta)J_x$, where $J_{x,y,z} = \frac{1}{2}\sum_i \sigma_i^{x,y,z}$ are collective-spin operators. We characterize the amount of spin squeezing through the parameter[3,30],

$$\xi_{\mathrm{R}}^2(t) = \frac{N\min_\theta(\mathrm{Var}(J_\theta))}{\langle J_y\rangle^2}, \qquad (2)$$

which quantifies the metrological gain in a Ramsey interferometry experiment. To measure $|\langle J_y\rangle|$, we simply rotate the state $|\psi(t)\rangle$ back to the z axis using a second $\pi/2$ pulse around x. To measure $\mathrm{Var}(J_\theta)$, we instead perform a microwave rotation around the y axis, where the angle θ is tuned by the duration of the pulse. Finally, we read out the state of each atom with a detection efficiency of 97.5% for $|\uparrow\rangle$ and 99% for $|\downarrow\rangle$ (Methods). Operationally, each experimental sequence is repeated roughly 200 times, and from this series of snapshots, we calculate the average and variance of all collective-spin operators. For a given interaction time, t, the noise distribution has a specific direction of smallest uncertainty, corresponding to the angle $\theta^*(t)$ that minimizes the variance of J_θ (Fig. 1b). Beginning with a 6×6 array, we measure $\mathrm{Var}(J_\theta)$ as a function of θ for $t = 0.3$ μs. As shown in Fig. 2a, the variance shows a sinusoidal shape that reveals the underlying elliptical distribution of the spin fluctuations and allows us to determine θ^*. We then investigate the time evolution of both $|\langle J_y\rangle|$ and $\mathrm{Var}(J_{\theta^*})$. As the system evolves, the initial coherent-spin state expands into a superposition of states (fan of red arrows, Fig. 1b), which causes the mean-spin length, $|\langle J_y\rangle|$ (red circles, Fig. 2b), to decay towards zero[26,27]. At the same time, the variance of J_θ (blue circles, Fig. 2b) initially decreases below its $t = 0$ value, reaches a minimum and then increases, exceeding its $t = 0$ value at late times[9].

Taken together, $|\langle J_y\rangle|$ and $\mathrm{Var}(J_{\theta^*})$ allow us to reconstruct the squeezing parameter ξ_{R}^2 (or $10\log_{10}(\xi_{\mathrm{R}}^2)$ when expressed in dB) as a function of time. As illustrated in Fig. 2b, the dynamics of the squeezing parameter are qualitatively similar to those of the variance: ξ_{R}^2 initially decreases below the SQL, reaches an optimum $\xi_{\mathrm{R}}^{2\star}$ at time t^* and then increases, exceeding the SQL at late times. The system remains in a squeezed state (that is, $\xi_{\mathrm{R}}^2 < 1$) for roughly 0.5 μs and shows an optimal squeezing parameter of -2.7 ± 0.3 dB. The optimal squeezing is highly sensitive to detections errors, and analytically correcting for these errors (diamond markers, Fig. 2 and Methods) leads to a minimum squeezing parameter of -3.9 ± 0.3 dB. However, even this corrected value does not reach the optimum (roughly −6.7 dB) predicted for the dipolar XY model. We attribute this to two other types of experimental imperfection, which also degrade the squeezing parameter: errors in the initial state preparation and imperfections in our microwave pulses. In contrast to detection errors, these imperfections directly affect the many-body squeezing dynamics (Methods); accounting for these further errors leads to significantly better agreement between theory and experiment (Fig. 2c).

At a fundamental level, a squeezing parameter $\xi_{\mathrm{R}}^2 < 1$ necessarily indicates the presence of entanglement in our system[31,32]. We quantify the entanglement depth as a function of time; an entanglement depth of k means that the many-body state cannot be written as a statistical mixture of states factorized into clusters containing up to $(k-1)$ particles: that is, at least one k-particle subsystem is entangled[32–34]. For a particular spin length, $|\langle J_y\rangle|$, the minimum attainable variance of the quantum state gives a lower bound on the entanglement depth[32]. Fixed contours of this bound for different values of k are shown in Fig. 2d: if a data point falls below the line labelled by k, the entanglement depth is thus at least $k+1$. The many-body dynamics of our system leads to a state whose entanglement depth increases rapidly at early times. Near the optimal squeezing time, t^*, the entanglement depth reaches a maximum of $k = 3$ (for the measurement-corrected data, we find $k = 5$) for our 36-atom system.

One of the distinguishing features of spin squeezing in all-to-all interacting models is that it is scalable—the optimal squeezing parameter, $\xi_{\mathrm{R}}^{2\star}$, scales non-trivially with system size as $N^{-\nu}$ with $\nu = 2/3$ (ref. 4). Whether this is the case for power-law interacting systems is significantly more subtle. A heuristic way to understand the emergence of early time squeezing dynamics in the dipolar XY model consists of rewriting the interaction as: $(\sigma_i^x\sigma_j^x + \sigma_i^y\sigma_j^y)/r_{ij}^3 = (\boldsymbol{\sigma}_i\cdot\boldsymbol{\sigma}_j - \sigma_i^z\sigma_j^z)/r_{ij}^3$; for our initial coherent-spin state, the Heisenberg term yields no dynamics, whereas the $\sigma_i^z\sigma_j^z/r_{ij}^3$ term approximates the squeezing dynamics generated by the all-to-all coupled, one-axis twisting (OAT) model $H_{\mathrm{OAT}} \propto \sum_{i,j}\sigma_i^z\sigma_j^z \propto J_z^2$, at short times[15,35]. However, this description breaks

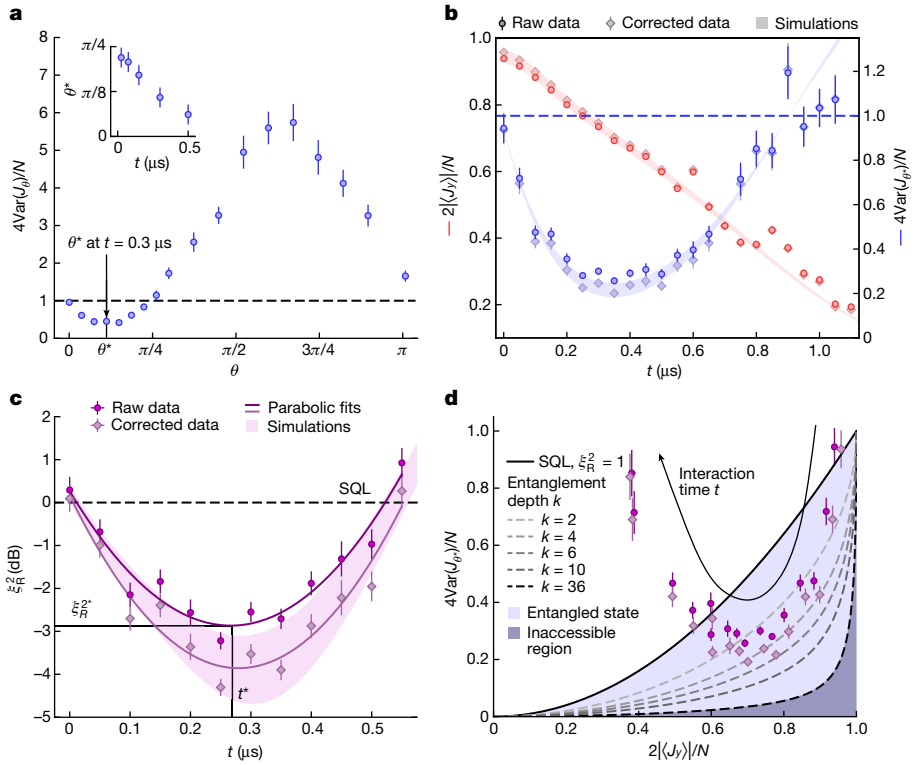

Fig. 2 | Dynamical evolution of spin squeezing in an $N = 6 \times 6$ array. **a**, Determination of the angle θ^* that minimizes the spin fluctuations for a fixed interaction time, $t = 0.3$ μs. The inset shows $\theta^*(t)$ determined for different times, t. The dashed line in **a** and **b** corresponds to the uncorrelated case $4\mathrm{Var}(J_\theta)/N = 1$. **b**, Measurements of the spin length $|\langle J_y\rangle|$ (red circles) and of the minimum variance $\mathrm{Var}(J_{\theta^*})$ (blue circles). The diamond markers are the data corrected for the detection errors, as described in the Methods. The shaded regions represent the results of the unitary spin dynamics, without any free parameter, including 97.5 ± 1% (99 ± 1%) detection efficiency for $|\uparrow\rangle$ ($|\downarrow\rangle$). **c**, Squeezing parameter $\xi_R^2(t)$ as a function of time. The solid curves are parabolic fits used to determine the optimal squeezing parameter $\xi_R^{2\star}$ and the optimal squeezing time t^*. As in **c**, the shaded area shows simulations including ±1% uncertainty in the detection efficiencies. **d**, Parametric plot of the variance as a function of the spin length. The coloured area, delimited by the black solid curve $\xi_R^2 = 1$, depicts the region where entanglement exists in the system. The grey dashed curves correspond to entanglement depths of k and the dashed black curve to a maximal entanglement depth of $k = 36$. The black arrow shows the direction of increasing interaction time.

down on an $\mathcal{O}(h/J)$ time scale (that is, as soon as the state is no longer fully polarized) and thus cannot explain the emergence of scalable spin squeezing. Going beyond this heuristic rewriting, more rigorous arguments can be made for the emergence of scalable spin squeezing in the dipolar XY Hamiltonian (Methods).

In particular, in power-law interacting systems, scalable spin squeezing has been recently conjectured to be closely related to CSB (ferromagnetic XY) order[6,7,9,10]. The mean-spin direction is the order parameter of such a system, and thus, in the ordered phase, it should equilibrate to some non-zero value; this is clearly a prerequisite for scalable squeezing, because the denominator of the squeezing parameter, ξ_R^2, is precisely the square of the mean-spin length, $\langle J_y\rangle^2$ (equation (2)). More subtly, the low-energy spectrum associated with ferromagnetic XY order is expected to consist of so-called Anderson towers, wherein the energy is proportional to J_z^2 (Methods)[36,37]. Crucially, this leads to the emergence and persistence of OAT-like dynamics even until late times, $t \sim \mathcal{O}(Nh/J)$; these dynamics twist the initial quantum fluctuations, shrinking the minimum variance in the yz plane (equation (2)), thus leading to scalable spin squeezing. Finally, let us emphasize that even this picture is only approximate: the eventual thermalization of the dipolar XY model implies that its dynamics (even at low energies) cannot be perfectly captured by OAT[10].

For the dipolar XY interactions that we investigate here, CSB, and thus scalable squeezing, is expected in $d = 2$ (refs. 6,7,9,10) but not in $d = 1$ (refs. 7,10). To this end, we measure the squeezing dynamics in systems ranging from $N = 2 \times 2$ to 10×10 atoms. In principle, determining the minimum squeezing parameter requires optimizing over both time and θ for each system size; as N increases, the optimal time, t^*, is expected to increase while the optimal θ^* is expected to decrease. Analogous to our previous procedure, we begin by extracting θ^* at a fixed time t, and measuring the time evolution of $|\langle J_y\rangle|$ and $\mathrm{Var}(J_{\theta^*})$; the time at which the variance is minimized provides a self-consistent way to experimentally verify that we are working near the two-parameter optimum.

As depicted in Fig. 3a, the dynamics of $|\langle J_y\rangle|$ at short times ($t < 0.25$ μs) collapse (that is, show a size-independent decay) for all N owing to rapid local relaxation of the magnetization (which can be analysed using spin-wave theory, Methods and ref. 38). At later times, $|\langle J_y\rangle|$ decreases more slowly for increasing system size, indicative of CSB order. The dynamics of the variance also depend on N (Fig. 3b): the minimum variance improves and occurs at later times as the system size increases. From these measurements, for each system size, we compute the squeezing dynamics and extract both the optimal squeezing parameter, $\xi_R^{2\star}$, and the corresponding optimal interaction time, t^*.

As previously mentioned, in the all-to-all interacting case, both optima are expected to scale with system size[4,39]. Recent theoretical work predicts that scalable squeezing can also arise in our 2D dipolar XY model[9,10,18]. This expectation is indeed borne out by our data. As shown in Fig. 3c,d, we find that $\xi_R^{2\star} \approx N^{-\nu}$ and $t^* \cong N^{\mu}$ with $\nu = 0.18(2)$ and $\mu = 0.32(3)$; when correcting for detection errors, we find that $\nu = 0.25(5)$, whereas μ does not change. The exponent that we observe

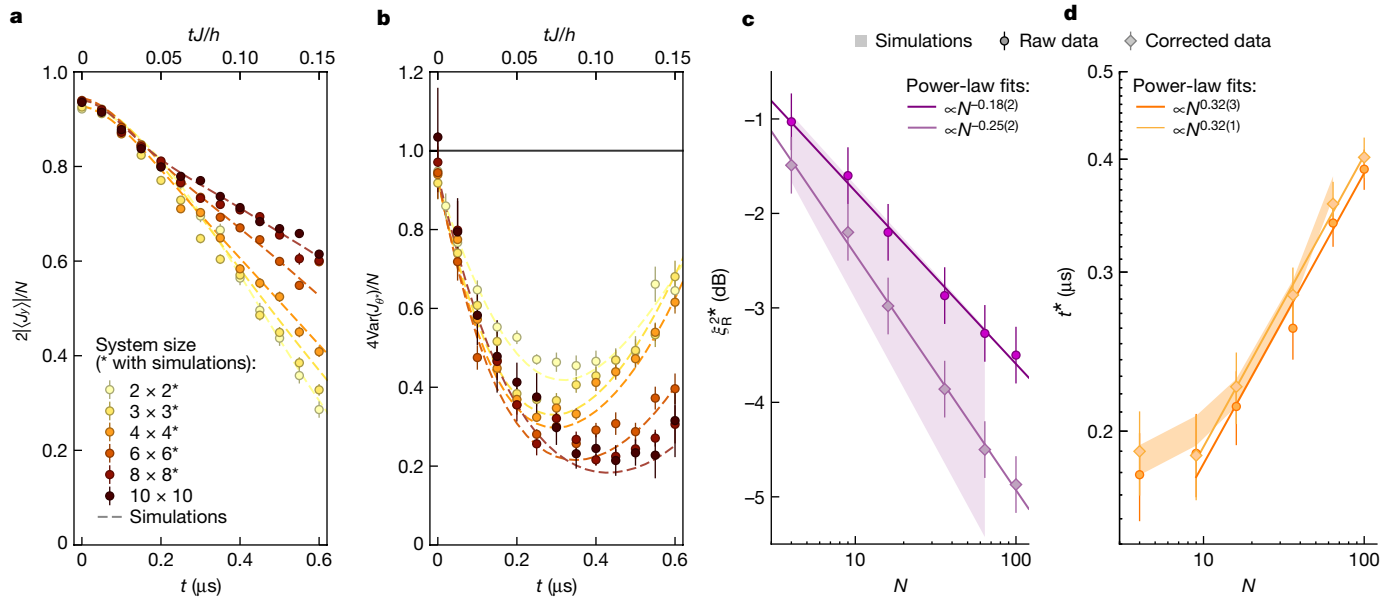

Fig. 3 | Scalable spin squeezing in the 2D, ferromagnetic, dipolar XY model. **a**,**b**, Measurement of the spin length $|\langle J_y \rangle|$ (**a**) and measurement of $\mathrm{Var}(J_{\theta^\star})$ (**b**) as a function of time for various system sizes. The dashed lines correspond to the results of matrix-product state simulations without any adjustable parameters, which are limited to system sizes of 8 × 8 (Methods). **c**,**d**, Minimum squeezing parameter $\xi_R^{2\star}$ (**c**) and associated optimal interaction time $t^\star$ (**d**), as a function of N. The circles and diamonds correspond to the raw and detection-error corrected data, respectively. The solid lines are power-law fits. The shaded regions are the results of the simulations for values of the detection efficiency of $|\uparrow\rangle$ ($|\downarrow\rangle$), 97.5 ± 1% (99 ± 1%), between their lower and upper limits.

for the optimal squeezing time is in agreement with that observed in the all-to-all coupled case, where $t^\star \approx N^{1/3}$ (ref. 4). However, the scaling of the optimal squeezing parameter is significantly weaker than that predicted for both all-to-all interactions, as well as the dipolar XY model[9,10]. Again, we attribute this to a combination of experimental imperfections, which, when accounted for, leads to a relatively good agreement between theory and experiment as shown in Fig. 3b,c. We note that this difference in agreement for $t^\star$ and $\xi_R^{2\star}$ is perhaps not unexpected; for example, measurement errors decrease the amount of achievable spin squeezing but do not change the optimal squeezing time.

As schematically depicted in Fig. 1b, the fact that squeezing shows an optimum in time arises from a competition between the generation of entanglement and the curvature of the Bloch sphere. Microscopically, the squeezing dynamics causes the coherent superposition of states to wrap around the Bloch sphere, but squeezing (equation (2)) is measured by means of the variance projected in the plane perpendicular to the mean-spin direction. Thus, the curvature of the Bloch sphere leads to a noise distribution that deviates from an elliptical shape[2] and manifests as additional variance (Methods). This suggests that one can improve the optimum squeezing by using a time-dependent protocol. In particular, by rotating the elliptical noise distribution towards the equator, one can minimize the impact of the projection on the measured variance[40,41].

To this end, working with a 6 × 6 array, we implement a discretized, single-step version of this protocol. We initialize the system in the same initial state, $|\psi(0)\rangle = |\rightarrow \cdots \rightarrow\rangle$, and let the squeezing dynamics proceed for $t = 0.13$ μs. Then, we perform a 25° rotation around the y axis to almost align the noise distribution's major axis parallel to the equator (Methods). The subsequent dynamics of the squeezing parameter are shown in Fig. 4 (green data). Three effects are observed. First, the optimal squeezing occurs at a later time, $t^\star \cong 0.45$ μs. Second, consistent with the intuition above, the system remains near its optimal squeezing value for roughly twice as long. Third, the value of the optimal squeezing parameter is improved by roughly 1 dB, reaching a value of −3.6 ± 0.3 dB.

To perform sensing, it is desirable to freeze the squeezing dynamics while acquiring the signal of interest. The simplest way to do so is to turn off the Hamiltonian. However, it is challenging to directly turn off the dipolar exchange interaction between the Rydberg atoms.

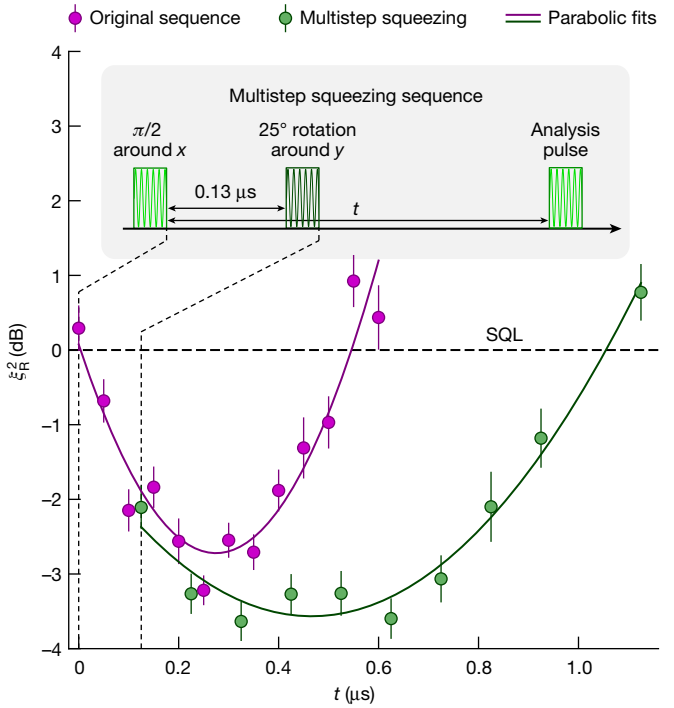

Fig. 4 | Multistep spin-squeezing protocol. Measurements of the squeezing parameter obtained with two different spin-squeezing protocols for a 6 × 6 array. The first one (purple dots) is the original sequence illustrated in Fig. 1c. The second one (dark green dots) is a multistep sequence depicted in the inset, where an extra 25° rotation pulse is used to rotate the elliptical noise distribution towards the equator. The solid curves are parabolic fits to guide the eye.

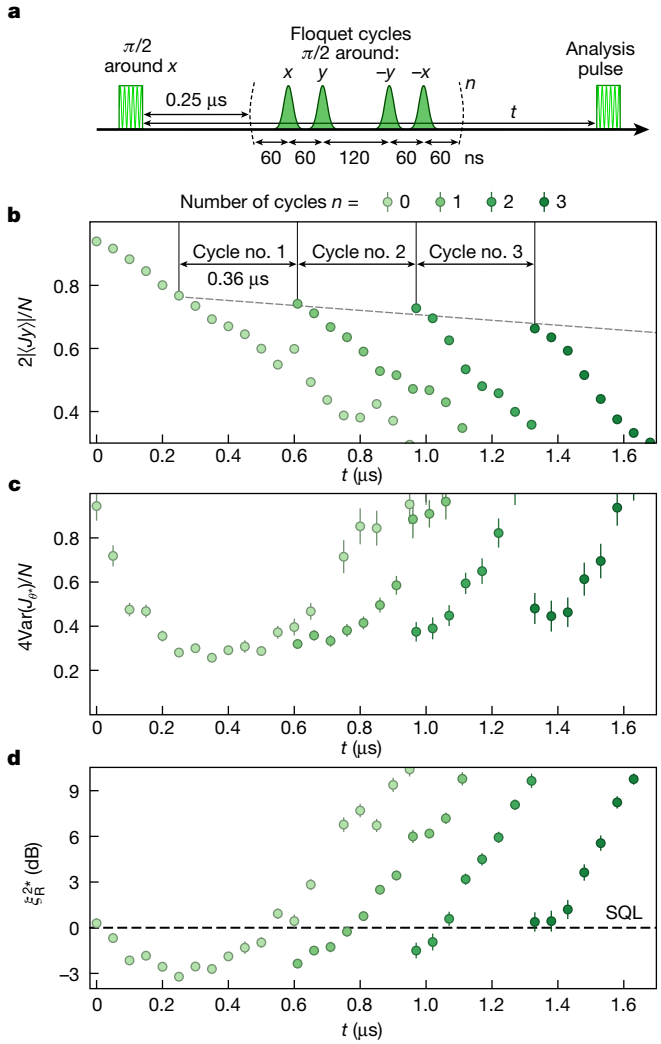

Fig. 5 | Floquet engineering to freeze spin squeezing. a, Experimental WAHUHA sequence using Floquet engineering to realize an effective dipolar Heisenberg interaction in a $N = 6 \times 6$ array. The system is periodically driven using n Floquet cycles, each composed of four $\pi/2$ Gaussian microwave pulses (of half-width 6.5 ns at $1/\sqrt{e}$), whose phases are chosen to realize rotations around the $(x, y, -y, -x)$ axes. **b**–**d**, Spin length $|\langle J_y\rangle|$ (**b**), minimal variance $\mathrm{Var}(J_{\theta^*})$ (**c**) and squeezing parameter ξ_R^2 (**d**) as a function of the total interaction time t for different numbers, n, of applied Floquet cycles. The grey dashed line in **b** is a guide to the eye to highlight the spin length measured immediately after each Floquet cycle.

To this end, we use an alternate approach, in which Floquet driving[26,27] engineers an effective dipolar Heisenberg interaction, $H_{\mathrm{Heis}} = -\frac{2J}{3}\sum_{i<j}\frac{a^3}{r_{ij}^3}\boldsymbol{\sigma}_i\cdot\boldsymbol{\sigma}_j$, from our original XY model. Crucially, the Heisenberg interaction commutes with all collective-spin operators, ensuring that: (1) it does not change the spin squeezing and (2) it does not affect the sensing signal associated, for example, to the presence of a uniform external field. (The Floquet sequence that generates the Heisenberg interaction leads to a rescaling of the strength of an external field by a factor of 1/3.)

To explore this behaviour, we let our system evolve to the optimal squeezing time and then attempt to freeze the dynamics by means of the Floquet WAHUHA sequence shown in Fig. 5a (ref. 42). A full Floquet cycle lasts $t_F = 0.36$ μs and for rapid driving, $Jt_F \ll 2\pi$, the time-averaged Hamiltonian is roughly H_{Heis} (ref. 27). We repeat this experiment for different numbers of Floquet cycles ranging from $n = 0$ to 3. The Floquet dynamics of $|\langle J_y\rangle|$ and $\mathrm{Var}(J_{\theta^*})$ are illustrated in Fig. 5b,c. For perfectly frozen dynamics, each set of curves (with different n) would simply be off-set in time from one another. This expectation is in good agreement with the data. Indeed, as depicted in Fig. 5b, we observe that the dynamics of $|\langle J_y\rangle|$ are translated in time, except for a small downwards drift (indicated by the grey dashed line). We note that this downwards drift is significantly weaker than the intrinsic dynamics of $|\langle J_y\rangle|$. Comparable behaviour is observed for $\mathrm{Var}(J_{\theta^*})$ (Fig. 5c). Finally, as illustrated by the squeezing parameter in Fig. 5d, the Floquet sequence prolongs the time scale over which squeezing remains below the SQL by nearly a factor three.

To conclude, our work represents the first observation, to our knowledge, of scalable spin squeezing in a many-body system with short-range, power-law interactions. It is complementary to the recent results obtained with Rydberg-dressed atoms[43,44] and long-range interactions in an ion string[45]. Our findings and methods are applicable to any quantum systems implementing the dipolar XY Hamiltonian, such as molecules[19–22] or solid-state spin defects[23]. Within the context of tweezer arrays, our work lays the foundation for several research directions. First, by generalizing our approach to alkaline-earth Rydberg tweezer arrays[46–48], it may be possible to map the spin squeezing from the Rydberg manifold to the so-called clock transition, to improve tweezer-based atomic clocks[49,50]. Second, by investigating squeezing as a function of the initial polarization, for example, by introducing disorder in the initial state preparation, it may be possible to test theoretical predictions that spin squeezing in short-range interacting systems is fundamentally distinct from that achieved in all-to-all coupled systems[10]. Finally, by implementing a continuous version of the multistep squeezing protocol, it may be possible to improve the scaling of the observed spin squeezing towards the Heisenberg limit.

Online content

Any methods, additional references, Nature Portfolio reporting summaries, source data, extended data, supplementary information, acknowledgements, peer review information; details of author contributions and competing interests; and statements of data and code availability are available at https://doi.org/10.1038/s41586-023-06414-9.

1. Giovannetti, V., Lloyd, S. & Maccone, L. Advances in quantum metrology. *Nat. Photon.* **5**, 222–229 (2011).
2. Pezzè, L., Smerzi, A., Oberthaler, M. K., Schmied, R. & Treutlein, P. Quantum metrology with nonclassical states of atomic ensembles. *Rev. Mod. Phys.* **90**, 035005 (2018).
3. Wineland, D. J., Bollinger, J. J., Itano, W. M., Moore, F. L. & Heinzen, D. J. Spin squeezing and reduced quantum noise in spectroscopy. *Phys. Rev. A* **46**, R6797–R6800 (1992).
4. Kitagawa, M. & Ueda, M. Squeezed spin states. *Phys. Rev. A* **47**, 5138–5143 (1993).
5. Ma, J., Wang, X., Sun, C. & Nori, F. Quantum spin squeezing. *Phys. Rep.* **509**, 89–165 (2011).
6. Perlin, M. A., Qu, C. & Rey, A. M. Spin squeezing with short-range spin-exchange interactions. *Phys. Rev. Lett.* **125**, 223401 (2020).
7. Comparin, T., Mezzacapo, F. & Roscilde, T. Robust spin squeezing from the tower of states of U(1)-symmetric spin Hamiltonians. *Phys. Rev. A* **105**, 022625 (2022).
8. Comparin, T., Mezzacapo, F., Robert-de Saint-Vincent, M. & Roscilde, T. Scalable spin squeezing from spontaneous breaking of a continuous symmetry. *Phys. Rev. Lett.* **129**, 113201 (2022).
9. Comparin, T., Mezzacapo, F. & Roscilde, T. Multipartite entangled states in dipolar quantum simulators. *Phys. Rev. Lett.* **129**, 150503 (2022).
10. Block, M. et al. A universal theory of spin squeezing. Preprint at https://arxiv.org/abs/2301.09636 (2023).
11. Tse, M. et al. Quantum-enhanced advanced LIGO detectors in the era of gravitational-wave astronomy. *Phys. Rev. Lett.* **123**, 231107 (2019).
12. Hosten, O., Engelsen, N. J., Krishnakumar, R. & Kasevich, M. A. Measurement noise 100 times lower than the quantum-projection limit using entangled atoms. *Nature* **529**, 505–508 (2016).
13. Pedrozo-Peñafiel, E. et al. Entanglement on an optical atomic-clock transition. *Nature* **588**, 414–418 (2020).
14. Robinson, J. M. et al. Direct comparison of two spin squeezed optical clocks below the quantum projection noise limit. Preprint at https://arxiv.org/abs/2211.08621 (2022).
15. Foss-Feig, M., Gong, Z.-X., Gorshkov, A. V. & Clark, C. W. Entanglement and spin-squeezing without infinite-range interactions. Preprint at https://arxiv.org/abs/1612.07805 (2016).
16. Gil, L. I. R., Mukherjee, R., Bridge, E. M., Jones, M. P. A. & Pohl, T. Spin squeezing in a Rydberg lattice clock. *Phys. Rev. Lett.* **112**, 103601 (2014).
17. Young, J. T., Muleady, S. R., Perlin, M. A., Kaufman, A. M. & Rey, A. M. Enhancing spin squeezing using soft-core interactions. *Phys. Rev. Res.* **5**, L012033 (2023).
18. Roscilde, T., Comparin, T. & Mezzacapo, F. Entangling dynamics from effective rotor/spin-wave separation in U(1)-symmetric quantum spin models. Preprint at https://arxiv.org/abs/2302.09271 (2023).

19. Yan, B. et al. Observation of dipolar spin-exchange interactions with lattice-confined polar molecules. *Nature* **501**, 521–525 (2013).
20. Bao, Y. et al. Dipolar spin-exchange and entanglement between molecules in an optical tweezer array. Preprint at https://arxiv.org/abs/2211.09780 (2022).
21. Holland, C. M., Lu, Y. & Cheuk, L. W. On-demand entanglement of molecules in a reconfigurable optical tweezer array. Peprint at https://arxiv.org/abs/2210.06309 (2022).
22. Christakis, L. et al. Probing site-resolved correlations in a spin system of ultracold molecules. *Nature* **614**, 64–69 (2023).
23. Wolfowicz, G. et al. Quantum guidelines for solid-state spin defects. *Nat. Rev. Mater.* **6**, 906–925 (2021).
24. de Léséleuc, S., Barredo, D., Lienhard, V., Browaeys, A. & Lahaye, T. Optical control of the resonant dipole-dipole interaction between Rydberg atoms. *Phys. Rev. Lett.* **119**, 053202 (2017).
25. Chen, C. et al. Continuous symmetry breaking in a two-dimensional Rydberg array. *Nature* **616**, 691–695 (2023).
26. Geier, S. et al. Floquet Hamiltonian engineering of an isolated many-body spin system. *Science* **374**, 1149–1152 (2021).
27. Scholl, P. et al. Microwave engineering of programmable *XXZ* Hamiltonians in arrays of Rydberg atoms. *PRX Quantum* **3**, 020303 (2022).
28. Scholl, P. et al. Quantum simulation of 2D antiferromagnets with hundreds of Rydberg atoms. *Nature* **595**, 233–238 (2021).
29. Browaeys, A. & Lahaye, T. Many-body physics with individually controlled Rydberg atoms. *Nat. Phys.* **16**, 132–142 (2020).
30. Wineland, D. J., Bollinger, J. J., Itano, W. M. & Heinzen, D. J. Squeezed atomic states and projection noise in spectroscopy. *Phys. Rev. A* **50**, 67–88 (1994).
31. Sørensen, A., Duan, L.-M., Cirac, J. I. & Zoller, P. Many-particle entanglement with Bose–Einstein condensates. *Nature* **409**, 63–66 (2001).
32. Sørensen, A. S. & Mølmer, K. Entanglement and extreme spin squeezing. *Phys. Rev. Lett.* **86**, 4431–4434 (2001).
33. Estéve, J., Gross, C., Weller, A., Giovanazzi, S. & Oberthaler, M. K. Squeezing and entanglement in a Bose-Einstein condensate. *Nature* **455**, 1216–1219 (2008).
34. Riedel, M. F. et al. Atom-chip-based generation of entanglement for quantum metrology. *Nature* **464**, 1170–1173 (2010).
35. Roscilde, T., Mezzacapo, F. & Comparin, T. Spin squeezing from bilinear spin-spin interactions: two simple theorems. *Phys. Rev. A* **104**, L040601 (2021).
36. Anderson, P. W. An approximate quantum theory of the antiferromagnetic ground state. *Phys. Rev.* **86**, 694–701 (1952).
37. Anderson, P. W. *Basic Notions Of Condensed Matter Physics* 1st edn (Westview Press/Addison-Wesley, 1997).
38. Roscilde, T., Comparin, T. & Mezzacapo, F. Rotor/spin-wave theory for quantum spin models with U(1) symmetry. Preprint at https://arxiv.org/abs/2303.00380 (2023).
39. Pezzé, L. & Smerzi, A. Entanglement, nonlinear dynamics, and the Heisenberg limit. *Phys. Rev. Lett.* **102**, 100401 (2009).
40. Muessel, W. et al. Twist-and-turn spin squeezing in Bose-Einstein condensates. *Phys. Rev. A* **92**, 023603 (2015).
41. Sorelli, G., Gessner, M., Smerzi, A. & Pezzè, L. Fast and optimal generation of entanglement in bosonic Josephson junctions. *Phys. Rev. A* **99**, 022329 (2019).
42. Waugh, J. S., Huber, L. M. & Haeberlen, U. Approach to high-resolution NMR in solids. *Phys. Rev. Lett.* **20**, 180–182 (1968).
43. Eckner, W. J. et al. Realizing spin squeezing with Rydberg interactions in a programmable optical clock. Preprint at https://arxiv.org/abs/2303.08078 (2023).
44. Hines, J. A. et al. Spin squeezing by Rydberg dressing in an array of atomic ensembles. Preprint at https://arxiv.org/abs/2303.08805 (2023).
45. Franke, J. et al. Quantum-enhanced sensing on an optical transition via emergent collective quantum correlations. Preprint at https://arxiv.org/abs/2303.10688 (2023).
46. Norcia, M. A., Young, A. W. & Kaufman, A. M. Microscopic control and detection of ultracold strontium in optical-tweezer arrays. *Phys. Rev. X* **8**, 041054 (2018).
47. Cooper, A. et al. Alkaline-earth atoms in optical tweezers. *Phys. Rev. X* **8**, 041055 (2018).
48. Saskin, S., Wilson, J. T., Grinkemeyer, B. & Thompson, J D. Narrow-line cooling and imaging of ytterbium atoms in an optical tweezer array. *Phys. Rev. Lett.* **122**, 143002 (2019).
49. Madjarov, I. S. et al. An atomic-array optical clock with single-atom readout. *Phys. Rev. X* **9**, 041052 (2019).
50. Young, A. W. et al. Half-minute-scale atomic coherence and high relative stability in a tweezer clock. *Nature* **588**, 408–413 (2020).

Methods

Experimental methods

The realization of the dipolar XY Hamiltonian relies on the ^{87}Rb Rydberg atom tweezer array platform described in previous works[28,51]. We encode our pseudo spin states as $|\uparrow\rangle = |60S_{1/2}, m_J = +1/2\rangle$ and $|\downarrow\rangle = |60P_{3/2}, m_J = -1/2\rangle$, and couple them by using microwaves at 17.2 GHz (Extended Data Fig. 1a). The microwave field is emitted by an antenna placed outside the vacuum chamber, leading to poor control over the polarization, due to the presence of metallic parts surrounding the atoms. To isolate the $|\uparrow\rangle - |\downarrow\rangle$ transition from irrelevant Zeeman sublevels we apply a roughly 45-G quantization magnetic field perpendicular to the array.

Experimental sequence. Extended Data Fig. 1b shows the details of the full experimental sequence. After randomly loading atoms into 1-mK deep optical tweezers (with a typical filling fraction of 60%), the array is assembled one atom at a time[51]. The atoms are then cooled to a temperature of 10 μK using Raman sideband cooling and optically pumped to $|g\rangle = |5S_{1/2}, F = 2, m_F = 2\rangle$. Following this, the power of the trapping light is adiabatically ramped down reducing the tweezer depth by a factor of roughly 50. Then, the tweezers are switched off and the atoms are excited to the Rydberg state $|\uparrow\rangle$. The excitation is performed by applying a two-photon stimulated Raman adiabatic passage with 421- and 1,013-nm lasers. To generate $|\psi(0)\rangle \equiv |\rightarrow\cdots\rightarrow\rangle$, we first apply a global resonant microwave $\pi/2$ pulse around x, with a Rabi frequency $\Omega = 2\pi \times 22.2$ MHz. After an interaction time t, an analysis microwave pulse is applied to change the measurement basis. When measuring the J_θ variance, the Rabi frequency of the analysis pulse is reduced down to $2\pi \times 4.1$ MHz to perform rotations with a higher angular resolution. We note that the $|\uparrow\rangle - |\downarrow\rangle$ transition frequency changes slightly when varying the microwave Rabi frequency. We attribute this to a light shift induced by couplings between the other components of the microwave polarization and the Zeeman sublevels of the $60S_{1/2}$ and $60P_{3/2}$ manifolds. We experimentally compensate for this effect by detuning the microwave (for example, for $\Omega = 2\pi \times 22.2$ MHz, the corresponding detuning is $2\pi \times 3.5$ MHz).

The experimental sequence (including detection, detailed below) is typically repeated for roughly 200 defect-free assembled arrays. This allows us to calculate the magnetization, spin correlations and variance by averaging over these realizations.

State-detection procedure. The detection protocol comprises three steps. In the first step, a 7.5 GHz microwave pulse (that is, the 'freezing pulse' in Extended Data Fig. 1) is used to transfer the spin population from $|\downarrow\rangle$ to the $n = 58$ hydrogenic manifold through a three-photon transition. Atoms in the hydrogenic states (labelled $|h_i\rangle$ in Extended Data Fig. 1b) are essentially decoupled from those remaining in $|\uparrow\rangle$, thus avoiding detrimental effects of interactions during the remainder of the read-out sequence. In the second step, a de-excitation pulse is performed by applying a 2.5 μs laser pulse on resonance with the transition between $|\uparrow\rangle$ and the short-lived intermediate state $6P_{3/2}$ from which the atoms decay back to $5S_{1/2}$. The final step consists of switching the tweezers back on to recapture and image (through fluorescence) only the atoms in $5S_{1/2}$ (while the others are lost). Thus we map the $|\uparrow\rangle$ (respectively $|\downarrow\rangle$) state to the presence (resp. absence) of the corresponding atom.

Experimental imperfections

Several sources of state preparation and measurement error contribute to increasing (that is, worsening) the observed squeezing parameter.

State preparation errors. The preparation sequence is composed of two steps: the Rydberg excitation (stimulated Raman adiabatic passage) and the preparation of $|\psi(0)\rangle$ by a microwave $\pi/2$ pulse. We estimate that the Rydberg excitation process is 98% efficient: on average, a fraction $\eta = 2\%$ of the atoms remains in the state $|g\rangle$ after excitation and hence do not participate in the dynamics. At the end of the sequence, these uninitialized atoms are imaged as a spin $|\uparrow\rangle$. The $\pi/2$-microwave pulse is also imperfect due to the unavoidable influence of the dipolar interactions between the atoms during its application. Including them in numerical simulations (Numerical simulations methods), we find that the collective-spin state undergoes a slight squeezing dynamics during the preparation pulse, which reduces the initial polarization by roughly 1%.

Measurement errors. Owing to the finite efficiency of each step in the read-out sequence (Extended Data Fig. 1b), an atom in $|\uparrow\rangle$ (resp. $|\downarrow\rangle$) has a non-zero probability $\epsilon_\uparrow$ (resp. $\epsilon_\downarrow$) to be detected in the wrong state[25]. The main contributions to $\epsilon_\uparrow$ are the finite efficiency $1 - \eta_{\mathrm{dx}}$ of the de-excitation pulse and the probability of loss ϵ due to collisions with the background gas. As for $\epsilon_\downarrow$, the main physical origin is the $|\downarrow\rangle$ Rydberg state radiative lifetime. We use a set of independent measurements and simulations to estimate these imperfections. We find to first order $\epsilon_\uparrow \cong \eta_{\mathrm{dx}} + \epsilon = 1.5\% + 1.0\% = 2.5\%$ and $\epsilon_\downarrow = 1.0\%$.

The finite detection errors impose a lower bound on the observed minimum variance. More specifically, the experimental magnetizations $\langle J_{y,\theta}\rangle$ and variance $\mathrm{Var}(J_\theta)$ are related to the same quantities $\langle \tilde{J}_{y,\theta}\rangle$ and $\mathrm{Var}(\tilde{J}_\theta)$ without detection errors by the following equations (valid to first order in $\epsilon_{\uparrow,\downarrow}$):

$$\begin{aligned}\langle J_{y,\theta}\rangle &= \frac{N}{2}(\epsilon_\downarrow - \epsilon_\uparrow) + (1 - \epsilon_\downarrow - \epsilon_\uparrow)\langle \tilde{J}_{y,\theta}\rangle \\ \mathrm{Var}(J_\theta) &= (1 - 2\epsilon_\downarrow - 2\epsilon_\uparrow)\mathrm{Var}(\tilde{J}_\theta) + \epsilon_\downarrow(N/2 - \langle \tilde{J}_\theta\rangle) \\ &\quad + \epsilon_\uparrow(N/2 + \langle \tilde{J}_\theta\rangle).\end{aligned} \tag{3}$$

By inverting the above equations, we calculate the mean-spin length and minimal variance free from detection errors (experimentally, the magnetization along the θ axis, not shown, verifies $|\langle J_\theta\rangle| \ll N/2$, leading to a negligible contribution to the correction). The data corrected in this way are shown as diamond symbols in the figures of the main text.

Numerical simulations methods

In this section, we provide a summary of the numerical methods used to simulate the experimental system and compare experimental findings and theoretical predictions.

Krylov simulations. For system sizes 2×2, 3×3 and 4×4, numerical simulations were performed with Krylov methods using Dynamite[52]. Krylov methods are extremely accurate over the short time scales relevant to the experiment, so the numerical error associated with this method is negligible. Moreover, it is straightforward to implement the aforementioned experimental imperfections in these simulations, including missing atoms, finite-duration pulses, measurement errors, positional disorder and van der Waals interactions (the last two sources of error were described in ref. 25 and have a negligible effect on the squeezing). We note that simulating missing atoms and positional disorder requires significant sampling, which we find converges after roughly 100 samples. Plugging the experimental parameters (interaction strengths, η and detection errors) into the numerics yields reasonable agreement with the data as shown, for example, in Figs. 2c and 3c. We attribute the remaining discrepancy to unaccounted for experimental imperfections: for example, the effects of other atomic levels outside the {↑, ↓, empty} manifold, decoherence or microwave control errors (resulting in roughly 3° of over or under rotation for $\Omega = 2\pi \times 4.1$ MHz).

Matrix-product operator evolution. For system sizes 6×6 and 8×8, we perform numerical simulations using exponential of matrix-product operators (MPO) as implemented in TenPy[53]. In this method, each step of time evolution is implemented as a MPO acting on the matrix-product

state, which increases the dimension of the matrices. Then, a truncation is implemented to approximate the quantum state in a new matrix-product form with a reduced matrix dimension. Typically, the accuracy of the method is controlled by the so-called bond dimension χ, that is, the maximum allowable dimension of the matrices in the simulation. As the entanglement increases during the quantum dynamics, a larger bond dimension is required to achieve the same level of accuracy. In the spin-squeezing dynamics at experimentally relevant system sizes, the optimal squeezing occurs at early times. As a result, we find good convergence for bond dimensions ranging from $\chi = 64$ to $\chi = 128$. We again implement the various imperfections discussed above to obtain reasonable agreement with the experimental results.

A larger bond dimension would be required to simulate the 10×10-atom system compared to the 8×8 one. Whereas the resulting increase in computational memory is affordable, the associated increase in computation time is severe. Specifically, going from simulating an 8×8 system with $\chi = 64$ to a 9×9 system with $\chi = 128$ increases the computation time from 2–3 to 8 days. This increase is partly due to the larger χ, and partly due to the fact that optimal squeezing occurs at a later time. For a 10×10 system, we estimate a required bond dimension of at least $\chi = 198$, leading to a simulation time of roughly 30 days. This corresponds to the time required for simulating a single disorder realization of the Hamiltonian; to simulate the experimental error tree, we must sample roughly 100 realizations, making matrix product state numerics on the 10×10 system impractical.

Time-dependent variational Monte Carlo. Making use of the time-dependent variational principle, we time-evolve a pair-product state (or spin-Jastrow state[7]), proved to be extremely accurate in describing the dynamics of the dipolar XY model[9]. For all system sizes, we simulate the dynamics with open boundary conditions, in the ideal case: that is, we consider the evolution starting from the perfect coherent-spin state, and driven exactly by the XY dipolar spin Hamiltonian.

Comparison between experimental results and numerical simulations

The results from all simulations are summarized in Extended Data Fig. 2, including various degrees of experimental imperfections. The good agreement between the data and the Krylov and MPO simulations including the state preparation and measurement errors shows that we understand most of the deviations between the experiment and the perfect dipolar XY dynamics. The simulations also highlight that even without detection errors, the imperfect state preparation contributes to the reduction of the squeezing parameter with respect to the perfect model.

As mentioned in the main text, although the experiment shows scalable squeezing, the observed scaling exponent is smaller than expected from the dipolar XY model. However, the results of the simulations for the perfect model indicates that the number of atoms used in the experiment ($N \leq 100$) only allows us to reach the onset of the predicted asymptotic scaling.

Emergence of OAT-like squeezing dynamics in the dipolar XY model

In this section, we elaborate on the approximation of the $d = 2$ dipolar XY model by the OAT model plus 'spin-wave' corrections (described below).

Projective approximation. The basis of this approximation is that the dynamics generated by the dipolar XY model, starting from a coherent-spin state is, projectively equivalent to that of the OAT model at short times. Indeed the initial coherent-spin state lives in the sector of Hilbert space possessing the maximal collective-spin of modulus $\mathbf{J}^2 = J(J+1)$ with $J = N/2$, which contains only permutationally symmetric states, that is, superpositions of Dicke states. Projecting onto this subspace, individual spin operators reduce to collective-spin operators, for example, $\mathcal{P}_{J=N/2}\sigma_i^\mu\mathcal{P}_{J=N/2} = 2J_\mu/N$ where $\mu = x, y, z$ and $\mathcal{P}_{J=N/2}$ is the projector on the Dicke-state manifold. Under the same projection, the dipolar XY Hamiltonian becomes equivalent to the OAT model: $\mathcal{P}_{J=N/2}H_{XY}\mathcal{P}_{J=N/2} = J_z^2/(2I) + \text{const.}$, where $1/(2I) = 2J[N(N-1)]^{-1}\sum_{i<j}(a/r_{ij})^3$ (refs. 18,38). This is nothing but an isolated Anderson tower[36,37], or, equivalently, a quantum rotor with macroscopic spin length $N/2$ and moment of inertia I (henceforth, 'rotor model').

The projective equivalence only holds under the assumption that the dipolar dynamics initialized in the Dicke-state manifold remains confined to it. This is clearly not the case, as the dipolar Hamiltonian (unlike the OAT) does not conserve $\mathbf{J}^2$. Nonetheless, CSB at the temperature corresponding to the initial coherent-spin state guarantees that the collective-spin modulus remains of $O(N^2)$, because the dynamics develops long-range spin–spin correlations. This suggests, therefore, that the evolved state may retain a large overlap with the Dicke manifold. Corrections to the projective equivalence picture can be added in the form of spin-wave excitations, which describe the component of the wavefunction leaking into sectors with $J < N/2$. Such corrections are addressed in the next subsection.

Spin-wave corrections. Here, we provide further insight on the demagnetization dynamics and its scaling properties with the atom number N, as observed in Fig. 3a. It relies on the rotor and spin-wave (RSW) theory[18,38], which allows one to write the magnetization as $\langle J_y\rangle = \langle J_y\rangle_R + \langle J_y\rangle_{SW}$. Here, $\langle J_y\rangle_R$ is the magnetization of the macroscopic spin of length $N/2$ (the rotor) introduced in the above. It obeys the dynamics of the OAT model $(J_z)^2/(2I)$; $\langle J_y\rangle_{SW}$ is a (negative) spin-wave (SW) contribution, coming from linear excitations at finite momentum that are triggered by the quantum quench dynamics.

RSW theory quantitatively accounts for the magnetization dynamics of systems with periodic boundary conditions, as shown by the excellent agreement with the time-dependent variational Monte Carlo results (Extended Data Fig. 3a)[18]. Owing to the very low density of spin-wave excitations triggered by the dipolar XY dynamics initialized in the coherent-spin state, the validity of RSW theory stretches to rather long times, well beyond those explored in our experiment. In particular, RSW theory explains the scaling properties of the magnetization dynamics at short times. As shown in the experimental data of Fig. 3a, as well as in the simulations in Extended Data Fig. 3a, the magnetization per spin shows an initial decay independent of system size up to a time scale $t_{SW} \cong 1/(4J)$. On the contrary, the later dynamics acquire a strong system-size dependence. RSW theory indicates that the initial size-independent decay comes from the proliferation of spin-wave excitations (appearing in counter-propagating pairs) at a time scale t_{SW} indicated by the first local minimum in Extended Data Fig. 3b, marking the saturation of the spin-wave population to its first maximum. By contrast, the later, size-dependent dynamics is dominated by the rotor variable, which depolarizes as in the OAT model, namely over time scales growing as $\sqrt{N}$. The longer persistence of magnetization for larger system sizes is the finite-size precursor of spontaneous symmetry breaking of the U(1) symmetry, which appears in the thermodynamic limit for both the OAT and dipolar XY models.

Multistep squeezing

In the main text, we implement the multistep squeezing protocol and demonstrate that it improves the optimal squeezing. Here, we provide further analysis from a theoretical perspective, as well as comparison between numerical simulation and experiments.

Physical intuition. The squeezing dynamics can be understood within a semiclassical picture[10]: treating the total spin as an ensemble of classical points, the initial state $|\psi(0)\rangle$ is represented by a Gaussian distribution with the same variance $\sqrt{N}$ along the z and x axes (that is,

a disc in the xz plane); in the dynamics, each point rotates around the z axis with an angular velocity proportional to its z polarization. The corresponding classical equations of motion are:

$$x(t) = x(0) + Nm_{xy} \sin\left(\frac{\tilde{J}\, zt}{N}\right), \qquad z(t) = z(0), \tag{4}$$

where $\tilde{J}$ and m_{xy} are the effective coupling strength and the effective total spin length. Consequently, the circle roughly deforms into an ellipse in the xz plane. However, the ellipse is perfect only for small z and short times, that is, $\tilde{J}\, zt \ll N$ and thus $N\sin(\tilde{J}\, zt/N) \approx \tilde{J}\, zt$ (Extended Data Fig. 4b). If such a condition were always satisfied, the squeezing parameter would keep improving for all time. Instead, the optimal squeezing is achieved when the deviation from a perfect ellipse (which happens at earlier times for larger z) becomes larger than the minor axis of the ellipse (Extended Data Fig. 4c). Therefore, a natural way to improve squeezing is to delay the time when such a deviation happens: before the deviation becomes the bottleneck, one can rotate the major axis of the ellipse towards the x axis (Extended Data Fig. 4d), so that the typical z value of the classical ensemble becomes smaller, delaying the non-elliptical deviation to later times (Extended Data Fig. 4e).

Comparison between numerics and experimental data. Similar to the single-step squeezing, we also performed time-evolving block decimation simulation for multistep squeezing dynamics, taking all experimental imperfections into account. The results are shown in Extended Data Fig. 5, where we observe a relatively good agreement between the numerics and the experimental data.

Data availability

The data are available from the corresponding author on reasonable request.

51. Barredo, D., de Léséleuc, S., Lienhard, V., Lahaye, T. & Browaeys, A. An atom-by-atom assembler of defect-free arbitrary two-dimensional atomic arrays. *Science* **354**, 1021–1023 (2016).
52. Kahanamoku-Meyer, G. D. & Wei, J. Gregdmeyer/dynamite: v.0.3.0. *Zenodo* https://doi.org/10.5281/zenodo.7622981 (2023).
53. Hauschild, J. & Pollmann, F. Efficient numerical simulations with tensor networks: tensor network Python (TeNPy). *SciPost Phys. Lect. Notes* https://scipost.org/10.21468/SciPostPhysLectNotes.5 (2018).

Acknowledgements We acknowledge the insights of and discussions with M. P. Zaletel, B. Halperin, B. Roberts, C. Laumann, E. Davis, S. Chern, W. Wu, Z. Wang, A.-M. Rey, F. Yang and Q. Liu. This work is supported by the Agence Nationale de la Recherche (ANR, project nos. RYBOTIN and ANR-22-PETQ-0004 France 2030, project no. QuBitAF), and the European Research Council (Advanced grant no. 101018511-ATARAXIA). B.Y. acknowledges support from the AFOSR MURI programme (grant no. W911NF-20-1-0136). M. Block acknowledges support through the Department of Defense through the National Defense Science and Engineering Graduate Fellowship Program. M. Bintz acknowledges support from the Army Research Office (grant no. W911NF-21-1-0262). N.Y.Y. acknowledges support from the US Department of Energy, Office of Science, National Quantum Information Science Research Centers, Quantum Systems Accelerator. D.B. acknowledges support from MCIN/AEI/10.13039/501100011033 (grant nos. RYC2018-025348-I, PID2020-119667GA-I00 and European Union NextGenerationEU PRTR-C17.I1). The computational results presented were performed in part using the Faculty of Arts and Sciences Research Computing (FASRC) Cannon cluster supported by the Faculty of Arts and Sciences (FAS) Division of Science Research Computing Group at Harvard University, the Savio computational cluster resource provided by the Berkeley Research Computing programme at the University of California and the Pôle Scientifique de Modélisation Numérique (PSMN) cluster at the ENS Lyon.

Author contributions G.B., G.E., C.C., J.A.B. and D.B. carried out the experiments. B.Y., M. Block, M. Bintz, T.C. and F.M. conducted the theoretical analysis and simulations. T.R., T.L., N.Y.Y. and A.B. supervised the work. All authors contributed to the data analysis, progression of the project and both the experimental and theoretical aspects. All authors contributed to the writing of the manuscript.

Competing interests A.B. and T.L. are cofounders and shareholders of PASQAL. The remaining authors declare no competing interests.

Additional information
Correspondence and requests for materials should be addressed to Cheng Chen.
Peer review information *Nature* thanks Joonhee Choi, Luming Duan and the other, anonymous, reviewer(s) for their contribution to the peer review of this work.
Reprints and permissions information is available at http://www.nature.com/reprints.

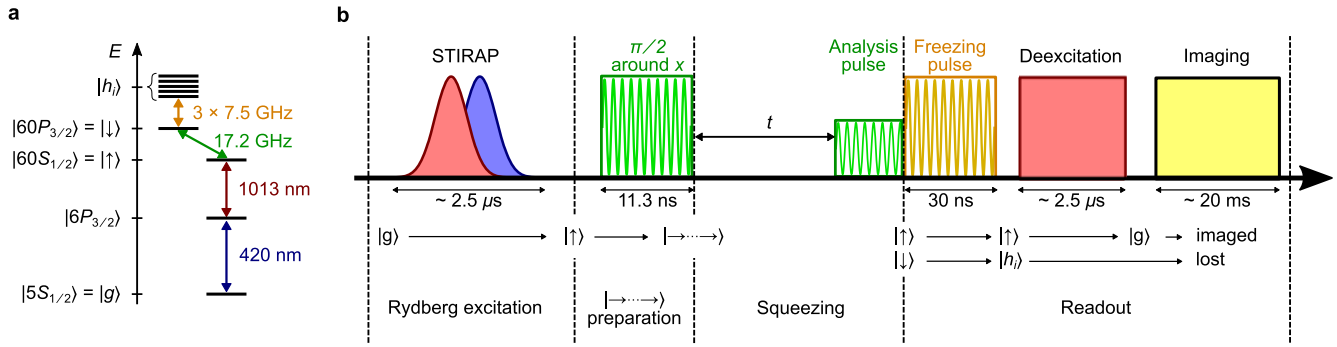

Extended Data Fig. 1 | Experimental sequence. a, Schematics of the atomic levels relevant for the experiment. **b**, Sequence of optical and microwave pulses (not to scale) used for all the experiments reported in Figs. 1, 2 and 3 of the main text.

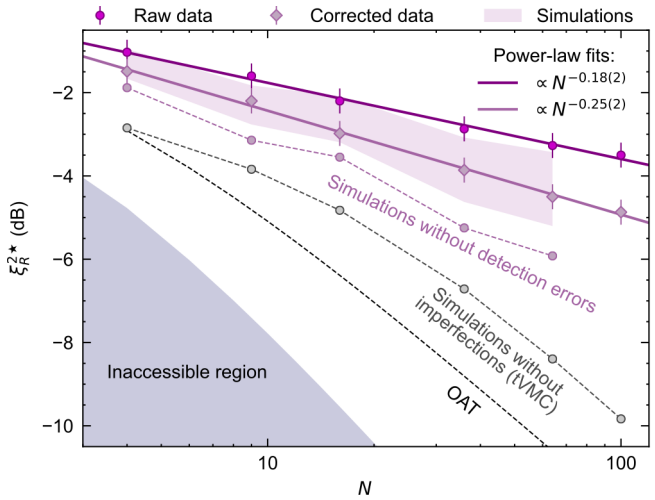

Extended Data Fig. 2 | Minimum squeezing parameter as a function of atom number *N*. The circles and diamonds correspond to raw and corrected data, respectively. The solid coloured lines are power-law fits. The purple shaded region shows the simulations including 97.5 ± 1% (resp. 99 ± 1%) detection efficiency of $|\uparrow\rangle$ (resp. $|\downarrow\rangle$). The dashed curves represent the results of simulations of the XY dipolar model without state preparation and measurement errors (grey) and without detection errors only (pink). The dashed black curve represents the exact results for the OAT model. The inaccessible region corresponds to values of the squeezing parameter smaller than $2/(2+N)^2$.

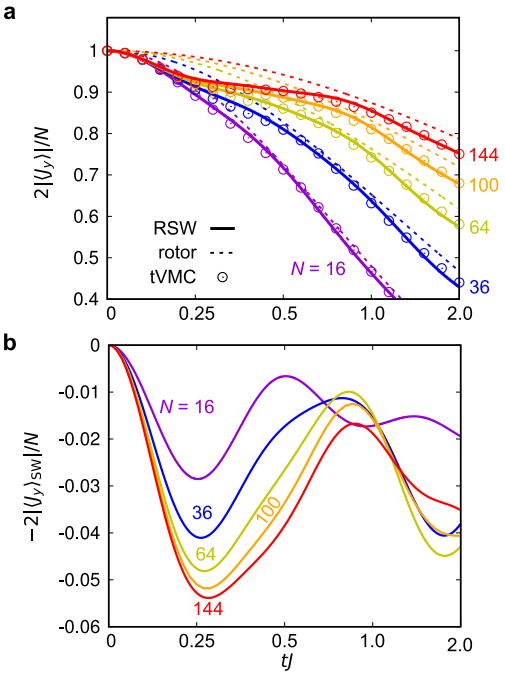

Extended Data Fig. 3 | Magnetization dynamics and its contributions. **a**, Dynamics of the magnetization per spin for the dipolar XY model on a periodic square lattice. Results from tVMC calculations and RSW theory for various system sizes ($N = 16, \ldots, 144$). We also show the rotor contribution to the magnetization, corresponding to an effective one-axis-twisting model (see text). **b**, Spin-wave (SW) contribution to the magnetization.

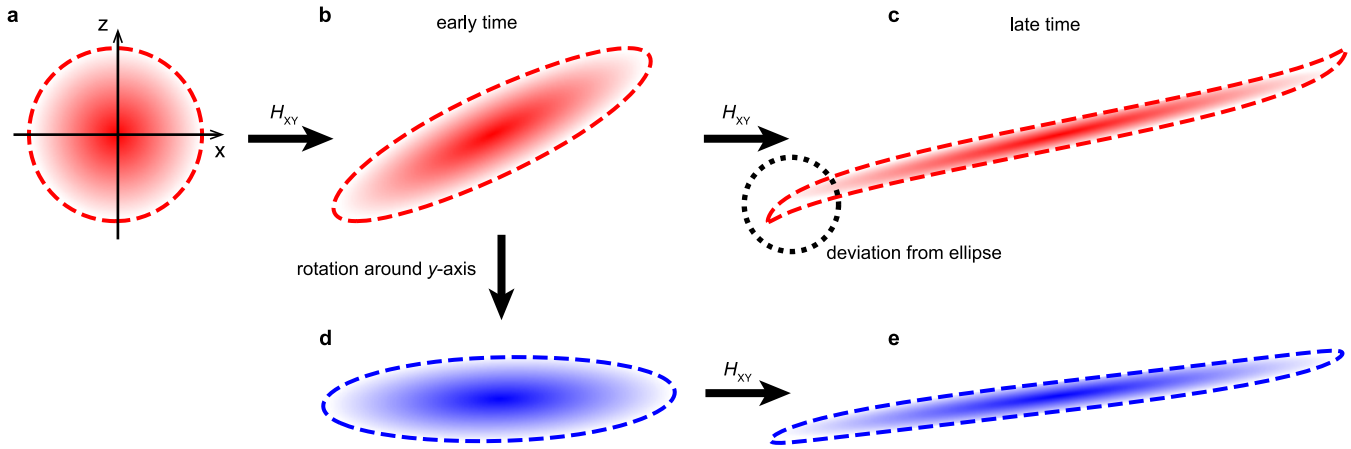

Extended Data Fig. 4 | Schematic depicting the multi-step squeezing protocol. a, Semi-classical description of a y-polarized initial state. **b**, **c**, Normal spin squeezing dynamics. **d**, **e**, Multi-step squeezing dynamics enabled by an extra rotation along the mean spin direction.

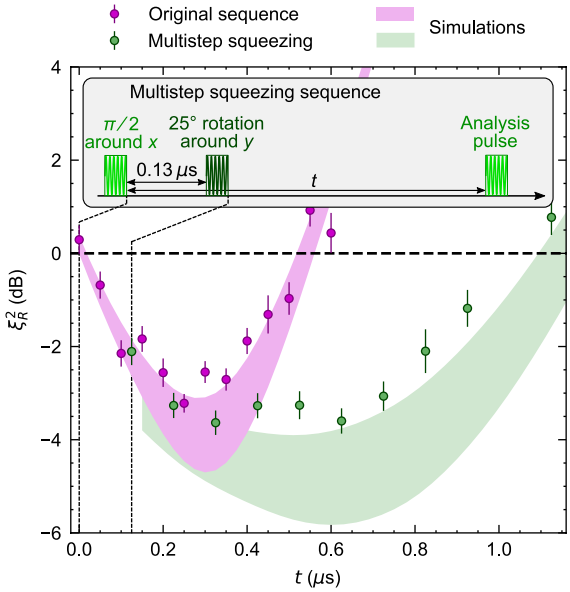

Extended Data Fig. 5 | Multistep squeezing, comparison between data and simulation. Measurements of the squeezing parameter obtained with two different procedures. The first one (purple dots) is the original sequence illustrated in Fig. 1(c). The second one (dark green dots) is the multistep sequence. The shaded regions show the simulations including 97.5 ± 1% (resp. 99 ± 1%) detection efficiency of $|\uparrow\rangle$ (resp. $|\downarrow\rangle$). These data correspond to a 6 × 6 array.